Reentrant transition in the shear viscosity of dilute rigid-rod dispersions

Hideki Kobayashi[*] and Ryoichi Yamamoto[†]

Department of Chemical Engineering, Kyoto University, Kyoto 615-8510, Japan and
CREST, Japan Science and Technology Agency, Kawaguchi 332-0012, Japan

The intrinsic viscosity of a dilute dispersion of rigid rods is studied using a recently developed direct numerical simulation (DNS) method for particle dispersions. A reentrant transition from shear-thinning behavior to the second Newtonian regime is successfully reproduced in the present DNS results around a Peclet number $Pe = 150$, which is in good agreement with our theoretical prediction of $Pe = 143$, at which the dynamic crossover from Brownian to non-Brownian behavior occurs in the rotational motion of the rotating rod. For $Pe > Pe_c$ at which the dynamic crossover occurs, the rigid rod undergoes non-Brownian rotational motion, which means that the rotational frequency is proportional to the shear rate. This crossover occurs only when the effect of the shear rate is dominant over the effect of the thermal fluctuation for all areas. Otherwise, the rotational motion is dominated by the thermal fluctuation. The viscosity undershoot is observed in our simulations before reaching the second Newtonian regime. The physical mechanisms behind these behaviors are analyzed in detail.

I. INTRODUCTION

The viscous properties of dilute dispersions of rigid rods change drastically as the rate of applied shear flows $\dot{\gamma}$ increases. Although many previous studies have investigated this phenomenon, the mechanism of this viscosity change is not yet completely clear. The aim of this paper is to contribute to the understanding of the detailed mechanism of the viscosity change by performing direct numerical simulations (DNSs) for a dilute dispersion of rigid rods that are subject to thermal fluctuations in a Newtonian host fluid.

The relationship between the measurable bulk rheological properties and the microscale description of dispersions of rodlike particles has been previously investigated [1–9]. Giesekus obtained the expression for the bulk stress tensor of diluted spheroidal dispersions under shear flow by taking into account the effects of the rotational Brownian motion of the spheroids caused by thermal fluctuations [3]. Leal and Hinch reported that the viscosity behavior is characterized by the aspect ratio l of the rod and the dimensionless shear rate $\dot{\gamma}/D_r$, where D_r is the rotational diffusion constant [5–8].

In the case of weak-shear flow, $\dot{\gamma}/D_r \ll 1$, the dilute rigid rod dispersions exhibit the first Newtonian behavior, in which the viscosity η of the dispersion is constant and equal to the first Newtonian (zero-shear limiting) value η_0. For an intermediate regime, $1 \ll \dot{\gamma}/D_r \ll l^3 + l^{-3}$, the dispersions exhibit shear-thinning behavior, in which $\eta \propto (\dot{\gamma}/D_r)^{-1/3}$. In the case of strong-shear flow, $l^3 + l^{-3} \ll \dot{\gamma}/D_r$, the dispersions reenter the second Newtonian regime, in which η becomes constant again and is equal to the second Newtonian (high-shear-limiting) value η_∞. Similar results have also been obtained in numerical [10,11] and experimental [12,13] studies. In this paper the phrase *viscosity transition* is used to express the changes in viscosity from the first Newtonian to shear-thinning behavior and from shear-thinning to the second Newtonian behavior. Similar results have been observed for dilute dispersions of flexible chains, both experimentally [14] and theoretically [15].

Hinch and Leal [5,6] proposed a theoretical model for the viscosity transitions. They considered that the viscosity η of the dispersion is determined by the ensemble average of the temporal viscosity $\hat{\eta}(\theta,\varphi)$ using the probability distribution function (PDF) $P_{\dot{\gamma}}(\theta,\varphi)$ of the two orientation angles θ and φ of the rod, i.e.,

$$\eta(\dot{\gamma}) = \int \hat{\eta}(\theta,\varphi)P_{\dot{\gamma}}(\theta,\varphi)\,d\theta\,d\varphi. \tag{1}$$

Here the form of $P_{\dot{\gamma}}(\theta,\varphi)$ is shear rate dependent, and the shear rate dependence of the dispersion viscosity $\eta(\dot{\gamma})$ is introduced mainly through this function.

The rigid rod undergoes a random rotational Brownian motion at low shear rates in the first Newtonian regime, in which the effect of thermal fluctuations is dominant over the effect of shear flow. Therefore,

$$P_{\dot{\gamma}}(\theta,\varphi) = \text{const} \tag{2}$$

holds over the entire phase space of θ and φ. The viscosity is thus constant with respect to the shear rate change in this regime, i.e., $\eta(\dot{\gamma}) = \eta_0$.

In contrast, the rigid rod undergoes a deterministic tumbling motion attributable to strong-shear flow in the second Newtonian regime. In this case, the tumbling motion is perfectly described by Jeffrey's equation [1]. Therefore, the PDF approaches the high-shear limiting (non-Brownian) asymptotic form with increasing $\dot{\gamma}$:

$$P_{\dot{\gamma}}(\theta,\varphi) = P_J(\theta,\varphi), \tag{3}$$

where $P_J(\theta,\varphi)$ is the theoretical result [6] derived from Jeffrey's equation [1]. The viscosity, therefore, tends to be constant again in this regime, i.e., $\eta = \eta_\infty$.

The viscosity exhibits strong shear-thinning behavior in the intermediate regime. The PDF is approximately given by

$$P_{\dot{\gamma}}(\theta,\varphi) \simeq P_J(\theta,\varphi) + (D_r/\dot{\gamma})P_1(\theta,\varphi), \tag{4}$$

[*]h-kobayashi@aist.go.jp
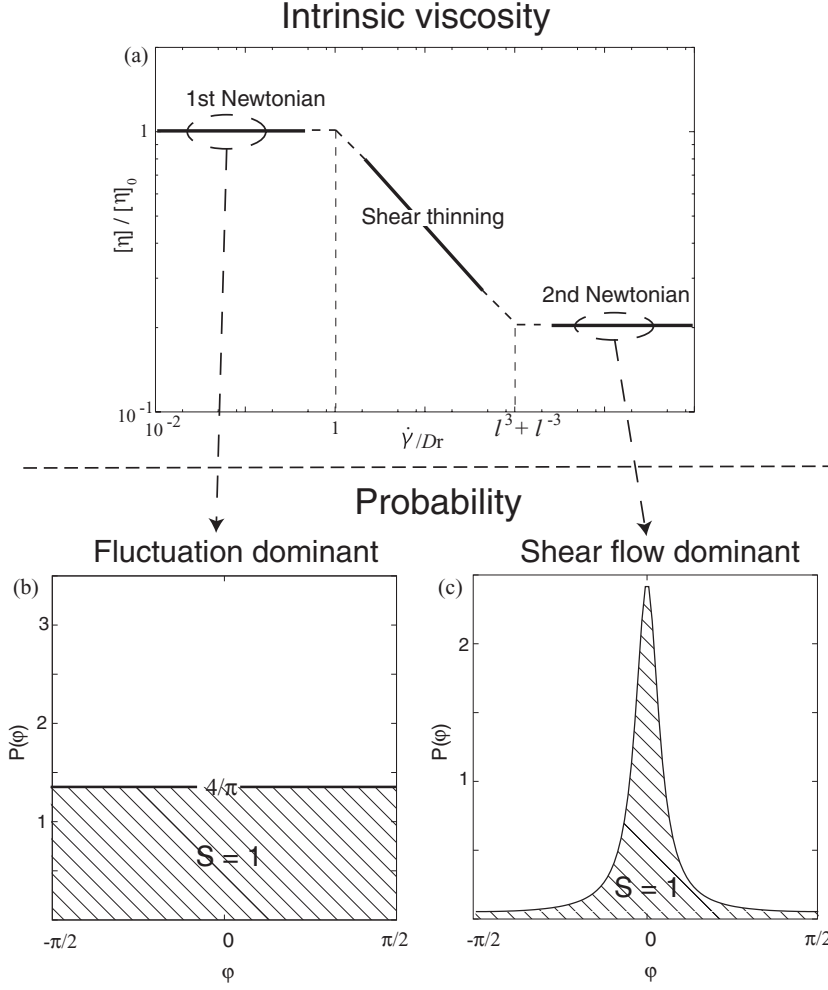[†]ryoichi@cheme.kyoto-u.ac.jp

FIG. 1. A schematic illustration of the viscosity transition. (a) A typical behavior of the intrinsic viscosity $[\eta]$ as a function of the dimensionless shear rate $\dot{\gamma}/D_r$. $[\eta]_0$ is the intrinsic viscosity in the limit $\dot{\gamma}/D_r \to 0$. Here $P(\varphi) \equiv \int_{-\frac{\pi}{2}}^{\frac{\pi}{2}} \cos\theta \, P(\theta, \varphi) \, d\theta$ is normalized so that $S \equiv \int_{-\frac{\pi}{2}}^{\frac{\pi}{2}} P(\varphi) \, d\varphi = 1$. (b) $P(\varphi)$ in the weak-shear regime where the rod undergoes random tumbling. (c) $P(\varphi)$ in the strong-shear regime where the rod undergoes periodic tumbling.

where P_1 represents the leading term of the perturbation expansion of the thermal effects. It is clearly seen that the contribution from the thermal effects decreases as the dimensionless shear rate $\dot{\gamma}/D_r$ increases in this regime, which gives rise to drastic shear-thinning behavior. The solid line shown in three different flow regimes in Fig. 1 represents a schematic illustration of the viscosity transition based on the above considerations.

Consistent with the theoretical model of Hinch and Leal [5,6], the viscosity transition from the first Newtonian to the shear-thinning regime has already been successfully reproduced in various numerical studies [11,16]. However, the viscosity transition from the shear-thinning to the second Newtonian regime has never been successfully reproduced by numerical simulations. For rigid rod dispersions, we did not find any previous studies that were performed at shear rates high enough to approach the second Newtonian regime. Several numerical simulations have been conducted for flexible chain dispersions at high shear rates that are expected to be in the second Newtonian regime. However, the viscosity transition from shear-thinning to the second Newtonian behavior has never been correctly reproduced, not even when the hydrodynamic interactions are taken into account using the Rotne-Prager-Yamakawa (RPY) tensor [16].

In the present study, we used a different type of approach, called the smoothed profile method (SPM) [17–21] categorized as a fluid mechanics approach [22], which can accurately take into account the thermal fluctuations and the hydrodynamic coupling between bead particles with a finite radius a and a Newtonian host fluid, based on DNS of particle dispersions. The viscosity of a rigid rod dispersion has been calculated using SPM to reproduce the viscosity transition from shear-thinning to the second Newtonian regime and to examine carefully the validity of the theoretical model proposed by Hinch and Leal [5,6].

II. METHODS

A. Model

We solve the dynamics of a single rigid rod in a Newtonian solvent using SPM [17–20]. In this method, the boundaries between solid particles and solvents are replaced with a continuous interface by assuming a smoothed profile. This simple modification enables us to calculate the hydrodynamic interactions both efficiently and accurately without neglecting many-body interactions. The equation governing a solvent with density ρ_f and shear viscosity η_f is a modified Navier-Stokes equation:

$$\rho_f \left[\frac{\partial \mathbf{u}}{\partial t} + (\mathbf{u} \cdot \nabla)\mathbf{u} \right] = \nabla \cdot \boldsymbol{\sigma} + \rho_f \phi \mathbf{f}_p + \mathbf{f}_{\text{shear}} \qquad (5)$$

with the incompressible condition $\nabla \cdot \mathbf{u} = 0$, where

$$\boldsymbol{\sigma} = -p\mathbf{I} + \eta_{\mathrm{f}}[\nabla \mathbf{u} + (\nabla \mathbf{u})^T] \tag{6}$$

is the Newtonian stress tensor with a solvent viscosity of η_f, and $\mathbf{u}(\mathbf{r},t)$ and $p(\mathbf{r},t)$ are the velocity and pressure fields of the solvent, respectively. A smoothed profile function $0 \leqslant \phi(\mathbf{r},t) \leqslant 1$ distinguishes between the fluid and particle domains, yielding $\phi = 1$ in the particle domain and $\phi = 0$ in the fluid domain. These domains are separated by thin interstitial regions, the thicknesses of which are given by ξ. The body force $\phi\mathbf{f}_\mathrm{p}$ is introduced so that the total velocity field $\mathbf{u}$ of the dispersion satisfies $\mathbf{u}(\mathbf{r}) = (1 - \phi)\mathbf{u}_\mathrm{f}(\mathbf{r}) + \phi\mathbf{u}_\mathrm{p}(\mathbf{r})$, where $\mathbf{u}_\mathrm{f}$ is the fluid velocity and $\mathbf{u}_\mathrm{p}$ represents the rigid motions of the particles. The incompressible condition $\nabla \cdot \mathbf{u}$ thus ensures $\nabla\phi \cdot (\mathbf{u}_\mathrm{p} - \mathbf{u}_\mathrm{f})$ because both $\mathbf{u}_\mathrm{f}$ and $\mathbf{u}_\mathrm{p}$ satisfy incompressible conditions. The gradient of ϕ is proportional to the surface-normal vector and has a support on the interfacial domains. Therefore, the body force $\phi\mathbf{f}_\mathrm{p}$ introduced to satisfy the rigidity of the particles ensures the appropriate impermeability boundary conditions at the fluid-particle interface, whereas the nonslip boundary conditions are imposed automatically by the viscous stress term in the Navier-Stokes equation. More detailed explanations and the mathematical expressions for ϕ and $\phi\mathbf{f}_\mathrm{p}$ were also detailed in our previous papers [17,18]. The external force $\mathbf{f}_\mathrm{shear}$ is introduced to maintain a linear shear with a shear rate of $\dot{\gamma}$. This force is applied with the oblique coordinate transformation based on tensor analysis [21,23].

In the present study, we use a bead-spring model consisting of N freely rotating beads in a single rigid rod. The bead diameter is $\sigma = 2a$. The motion of the ith bead is governed by the following Newton-Euler equations of motion with thermal fluctuations:

$$M_i \frac{d}{dt}\mathbf{V}_i = \mathbf{F}_i^\mathrm{H} + \mathbf{F}_i^\mathrm{P} + \mathbf{F}_i^C + \mathbf{G}_i^V, \quad \frac{d}{dt}\mathbf{R}_i = \mathbf{V}_i, \tag{7}$$

$$\mathbf{I}_i \cdot \frac{d}{dt}\boldsymbol{\Omega}_i = \mathbf{N}_i^\mathrm{H} + \mathbf{G}_i^\Omega, \tag{8}$$

where $\mathbf{R}_i$, $\mathbf{V}_i$, and $\boldsymbol{\Omega}_i$ are the position, translational velocity, and rotational velocity of the beads, respectively. The variables M_i and $\mathbf{I}_i$ are the mass and moment of inertia, and $\mathbf{F}_i^\mathrm{H}$ and $\mathbf{N}_i^\mathrm{H}$ are the hydrodynamic force and torque exerted by the solvent on the beads, respectively [17,18]. $\mathbf{G}_i^V$ and $\mathbf{G}_i^\Omega$ are the random force and torque, respectively, caused by thermal fluctuations. The temperature of the system is defined such that the long-time diffusive motion of dispersed particles reproduces the correct behavior [19,20]. $\mathbf{F}_i^\mathrm{P}$ represents the potential force attributable to direct interbead interactions.

From our previous study [21], we can evaluate the average stress tensor of the dispersion $\langle\boldsymbol{\sigma}^\mathrm{dis}\rangle$ as

$$\langle\boldsymbol{\sigma}^\mathrm{dis}\rangle = \langle\boldsymbol{\sigma}\rangle - \frac{1}{V}\left\langle\int d\mathbf{r}\mathbf{r}\rho\phi\mathbf{f}_p\right\rangle_t \tag{9}$$

with the volume $V = L_x L_y L_z$, where L_i is the system size in the i direction, $\langle\cdots\rangle$ denotes averaging over space and time, and $\langle\cdots\rangle_t$ denotes time averaging over the steady state.

We use a bead-spring model as a model of rodlike objects with a truncated Lennard-Jones potential and a finitely

extensible nonlinear elastic (FENE) potential. The truncated Lennard-Jones interaction is expressed in terms of U_LJ:

$$U_\mathrm{LJ}(r_{ij}) = \begin{cases} 4\epsilon\left[\left(\frac{\sigma}{r_{ij}}\right)^{12} - \left(\frac{\sigma}{r_{ij}}\right)^6\right] + \epsilon & \left(r_{ij} < 2^{\frac{1}{6}}\sigma\right) \\ 0 & \left(r_{ij} > 2^{\frac{1}{6}}\sigma\right), \end{cases} \tag{10}$$

where $r_{ij} = |\mathbf{R}_i - \mathbf{R}_j|$. The parameter ϵ characterizes the strength of the interactions, and σ represents the diameter of the beads. Consecutive beads on a chain are connected by a FENE potential of the form

$$U_\mathrm{FENE}(r) = -\frac{1}{2}k_\mathrm{c}R_0^2 \ln\left[1 - \left(\frac{r}{R_0}\right)^2\right], \tag{11}$$

where $r = |\mathbf{R}_{i+1} - \mathbf{R}_i|$, $k_c = 30\epsilon/\sigma^2$, and $R_0 = 1.5\sigma$. Let us denote $\mathbf{F}_i^C$ as the constraint force acting on the ith bead attributable to the bond-angle constraints that cause the connected beads to form a straight rod. Thus,

$$\mathbf{F}_i^C = \frac{\partial}{\partial\mathbf{R}_i}\left(\sum_{\alpha=3}^N \boldsymbol{\mu}_\alpha \cdot \boldsymbol{\Psi}_\alpha\right), \tag{12}$$

$$\boldsymbol{\Psi}_\alpha = (\alpha - 2)\mathbf{R}_1 - (\alpha - 1)\mathbf{R}_2 + \mathbf{R}_\alpha, \tag{13}$$

where $\boldsymbol{\Psi}_\alpha = 0$ is the constraint condition to be satisfied. The variable $\boldsymbol{\mu}_\alpha$ is a Lagrange multiplier associated with the constraints chosen such that the condition $\boldsymbol{\Psi}_\alpha = 0$ is satisfied at a time $t + h$, where h is the time increment of a single simulation step.

The numerical simulations are performed in three dimensions with periodic boundary conditions. The lattice spacing Δ is taken to be the unit of length. The unit of time is given by $\rho_f\Delta^2/\eta_f$, where $\eta_f = 1$ and $\rho_f = 1$. The system size is $L_x \times L_y \times L_z = 32 \times 32 \times 32$. The other parameters include the following: $\sigma = 4$, $\xi = 2$, $\epsilon = 1$, $M_i = 4\pi a^3/3$, $N = 5$, and $h = 6.7 \times 10^{-2}$. In the presented simulations under shear flow, the Navier-Stokes equation is discretized with a dealiased Fourier spectral scheme in space and with a Euler scheme in time [21]. To follow the motions of the beads, the positions, velocities and angular velocities of the beads are integrated with the Adams-Bashforth scheme. The bead particles are assumed to be neutrally buoyant, and hence no gravity effects are considered. At $t = 0$, the rigid rod aligns along the x axis, which is the flow direction. The total duration τ_t of each simulation is set such that $\dot{\gamma}\tau_t \simeq 3500$. The range of $k_\mathrm{B}T$ is $5.0 \times 10^{-4} < k_\mathrm{B}T < 32$ and that of $\dot{\gamma}$ is $5.0 \times 10^{-3} < \dot{\gamma} < 2.0 \times 10^{-2}$, where k_B is the Boltzmann constant, and T is the temperature. From the symmetry of the system, we follow the polar angles θ and φ defined in Fig. 2 to consider the motion of a rigid rod. The angle defined between the rod and the x-y plane is denoted by θ, and the angle defined between the rod projected on the x-y plane and the x axis is denoted by φ.

B. Effective aspect ratio

In the present study, the rigid rod is represented as connected beads. Because the beads composing the rod can rotate freely, the effective aspect ratio l differs from the simple geometrical aspect ratio L/σ, where $L \simeq N\sigma$ is the rod's length. Instead, we evaluate l numerically with the PDF of
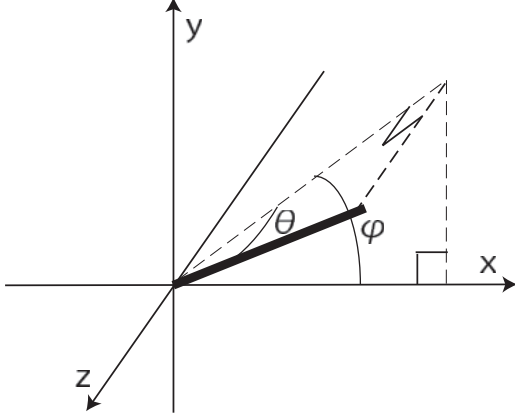
FIG. 2. The geometry of the rod's orientation in the present simulations.

the rotating rigid rods without thermal fluctuations in the x-y plane, i.e., $\theta = 0$, as represented by

$$P_J(\varphi) = \frac{C_0}{\frac{l^2-1}{l^2+1}\sin^2\varphi + \frac{1}{l^2+1}}, \tag{14}$$

where C_0 is determined from the normalization condition $\int_{-\frac{\pi}{2}}^{\frac{\pi}{2}} P_J(\varphi)\,d\varphi = 1$ [1]. Equation (14) was obtained in the following manner. The projection of the PDF $P_J(\varphi)$ of a rotating rigid rod on the x-y plane is governed by a Fokker-Planck equation of the form

$$\frac{\partial P_J(\varphi)}{\partial t} = \frac{\partial[\omega P_J(\varphi)]}{\partial \varphi} + 2D_r\frac{\partial P_J(\varphi)}{\partial \varphi^2}, \tag{15}$$

where $\omega = \dot{\varphi}$ is the angular velocity of the tumbling rod. When the rigid rod rotates in the x-y plane without thermal fluctuations in steady state, the Fokker-Planck equation is modified to

$$\frac{\partial[\omega P_J(\varphi)]}{\partial \varphi} = 0. \tag{16}$$

In this case, ω is represented as

$$\omega = \dot{\gamma}\left(\frac{l^2-1}{l^2+1}\sin^2\varphi + \frac{1}{l^2+1}\right) \tag{17}$$

from Jeffrey's equation [1]. Equation (14) is obtained because $P_J(\varphi)$ is inversely proportional to ω. Figure 3 shows that our numerical results of $P'(\varphi) = \int\cos\theta\, P_{\dot{\gamma}}(\theta,\varphi)\,d\theta$ of the strong-shear regime agree well with $P_J(\varphi)$ with $l = 7.1$. We thus use $l = 7.1$ for the present rigid rod, which is composed of freely rotating beads.

C. Analytic formula for the viscosity

Hinch and Leal [5,6] studied the rheological properties of a dilute dispersion of rigid nonspherical particles in steady shear flow. They obtained an analytical formula for the dispersion viscosity $\eta \equiv \sigma_{12}^{\mathrm{dis}}/\dot{\gamma}$. We analyze our numerical results using their formula. The dispersion viscosity η is given by the ensemble average of the temporal viscosity $\hat{\eta}(\theta,\varphi)$ using the
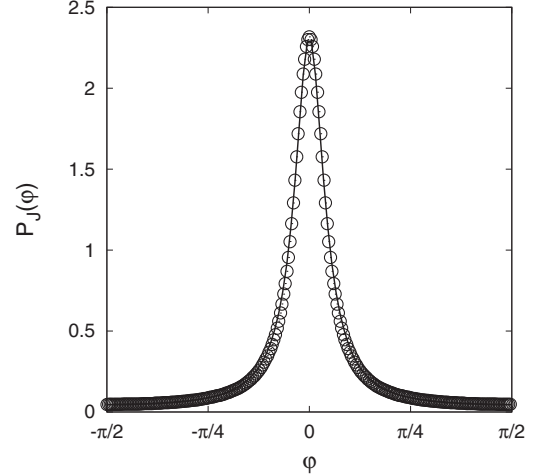

FIG. 3. The PDF for a rotational rigid rod as a function of φ without thermal fluctuations. Numerical results (open circle) and Eq. (14) with $l = 7.1$ (solid line).

PDF of the two angles for the rotating rigid rods $P_{\dot{\gamma}}(\theta,\varphi)$, which satisfies the normalization condition,

$$\int_{-\frac{\pi}{2}}^{\frac{\pi}{2}} \cos\theta\, d\theta \int_{-\frac{\pi}{2}}^{\frac{\pi}{2}} d\varphi\, P_{\dot{\gamma}}(\theta,\varphi) = 1. \tag{18}$$

The temporal shear viscosity is found to be

$$\hat{\eta}(\theta,\varphi) = \eta_f\left[1 + \Phi\left(A\cos^4\theta\sin^2 2\varphi + 2B\cos^2\theta + \frac{2}{I_3}\right.\right.$$
$$\left.\left. + \frac{D_r}{\dot{\gamma}}F\frac{1}{2}\cos^2\theta\sin 2\varphi\right)\right], \tag{19}$$

where Φ is the volume fraction of suspended particles, D_r is the rotational diffusion constant, and A, B, F, I_3 are the shape functions given in previous studies [4–6]. In the case of rigid rods, A, B, F, and I_3 are dependent only on the aspect ratio l at $l = 7.1$, $A = 8.44$, $B = 0.06$, and $I_3 = 0.99$.

The shear viscosity of the dispersion is obtained by substituting Eq. (19) into Eq. (1). When we consider the strong-shear case $D_r \ll \dot{\gamma}$, we can safely neglect the final term in Eq. (19). The dynamics of the angle φ become decoupled from the angle θ because the angle θ is sufficiently small for a large l [6]. Thus, we obtain the following formula:

$$\eta(\dot{\gamma}) = \int \hat{\eta}(\theta,\varphi)P''(\theta)P'(\varphi)\,d\theta\,d\varphi \tag{20}$$

$$= \eta_f\left[1 + \Phi\left(A\langle\cos^4\theta\rangle_\theta\langle\sin^2 2\varphi\rangle_\varphi + 2B\langle\cos^2\theta\rangle_\theta\right.\right.$$
$$\left.\left. + \frac{2}{I_3} + \Delta E\right)\right], \tag{21}$$

where $\langle f(\theta)\rangle_\theta = \int_{-\frac{\pi}{2}}^{\frac{\pi}{2}}\cos\theta\, d\theta f(\theta)P''(\theta)$, $\langle g(\varphi)\rangle_\varphi = \int_{-\frac{\pi}{2}}^{\frac{\pi}{2}} d\varphi g(\varphi)P'(\varphi)$, $P''(\theta) \equiv \int_{-\frac{\pi}{2}}^{\frac{\pi}{2}} P_{\dot{\gamma}}(\theta,\varphi)\,d\varphi$, and ΔE is the error arising from the separation of integrals over θ and φ. We can neglect ΔE safely because ΔE is sufficiently small in comparison with the other terms.
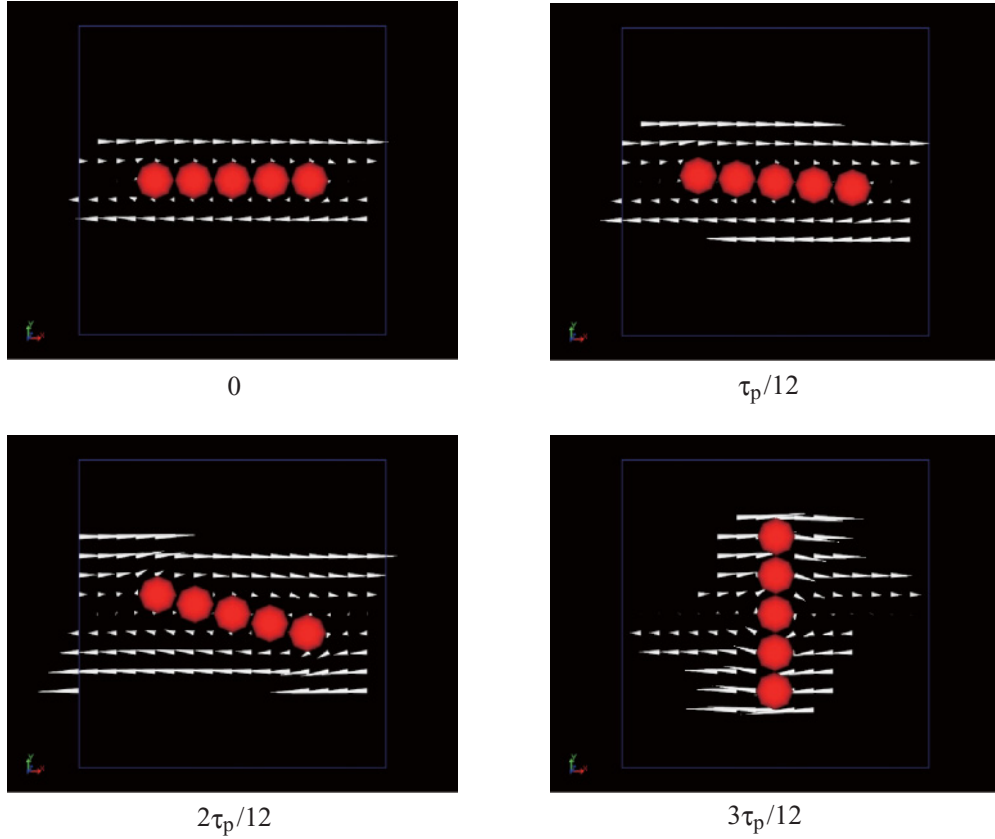
FIG. 4. (Color online) The time evolution of the fluid velocity field **u** at $k_BT = 0$. The times range from 0 to $\tau_p/4$, where τ_p is the rotational period. The velocity fields are plotted only when $|\mathbf{u}_d|/|\mathbf{u}| > 0.05$, where $\mathbf{u}_d$ is the deviation velocity field $\mathbf{u} - \dot{\gamma}(y - L_y/2)\mathbf{e_x}$.

III. RESULTS

Figure 4 shows the time evolution of the fluid velocity field **u** for $k_BT = 0$. Display of the velocity field, depicted by arrows, is limited to regions where the quantity $|\mathbf{u}_d|/|\mathbf{u}|$ exceeds 0.05, where $\mathbf{u}_d$ is the deviation velocity field defined as $\mathbf{u} - \dot{\gamma}(y - L_y/2)\mathbf{e_x}$. The time interval displayed is from 0 to $\tau_p/4$, where $t = 0$ is the time at which $\varphi = 0$ and τ_p is the rotational period. The rigid rod aligns almost fully with the shear direction in most of period. This motion is in good agreement with Jeffrey's equation [1]. The velocity **u** is approximately equal to $\dot{\gamma}(y - L_y/2)\mathbf{e_x}$ except in the vicinity of the rod. To examine the deviation velocity, we plot the time evolution of the deviation velocity field $\mathbf{u}_d$ in Fig. 5 in regions where $|\mathbf{u}_d|/|\mathbf{u}| > 0.05$. The amplitude of $\mathbf{u}_d$ is significant only near the rod. This is because the deviation velocity is attributable to an exchange of momentum between the particle and fluid. The amplitude of $\mathbf{u}_d$ at time $2\tau_p/12$ is larger than at $t = 0, \tau_p/4$. This behavior is in qualitative agreement with that of $\hat{\eta}(\theta, \varphi)$ which, as Eq. (19) reveals, has minima at $\varphi = 0, \pi/2$ and a maximum at $\varphi = \pi/4$. The momentum exchange between particle and fluid is clearly evident in $\hat{\eta}(\theta, \varphi)$.

In Fig. 6 we plotted the intrinsic viscosity

$$[\eta] \equiv \frac{\eta - \eta_f}{\eta_f \Phi} \qquad (22)$$

of the dispersion obtained from the present simulations as a function of the Peclet number Pe. Pe is the dimensionless

number that represents the strength of the shear flow normalized by the strength of diffusion caused by thermal fluctuations. In our work, Pe is defined as

$$\text{Pe} = \frac{6\pi\eta_f\sigma^3\dot{\gamma}}{k_BT}. \qquad (23)$$

We find that the intrinsic viscosity $[\eta]$ gradually changes from non-Newtonian (shear-thinning) to Newtonian behavior with increasing Peclet number, as shown in Fig. 6. The present simulation data for $[\eta]$ show shear-thinning behavior for $\text{Pe} < 10^2$ and second Newtonian behavior for $10^4 < \text{Pe}$. These results are in good agreement with previous theoretical studies [5,6,9].

To quantitatively compare our results with those of Hinch and Leal [5,6], we obtain the relationship between Pe in our definition and $\dot{\gamma}/D_r$, which is used in Hinch and Leal's work [5] instead of Pe. On the basis of the shell model [24,25], the rotational diffusion constant D_r for a rigid rod is calculated as

$$D_r = \frac{3[\ln l + d(l)]k_BT}{\pi\eta_f L^3}, \qquad (24)$$

$$d(l) = -0.662 + \frac{0.917}{l} - \frac{0.05}{l^2}. \qquad (25)$$

In the shell model mentioned above, the contour of the macromolecules of arbitrary shape is represented by a shell
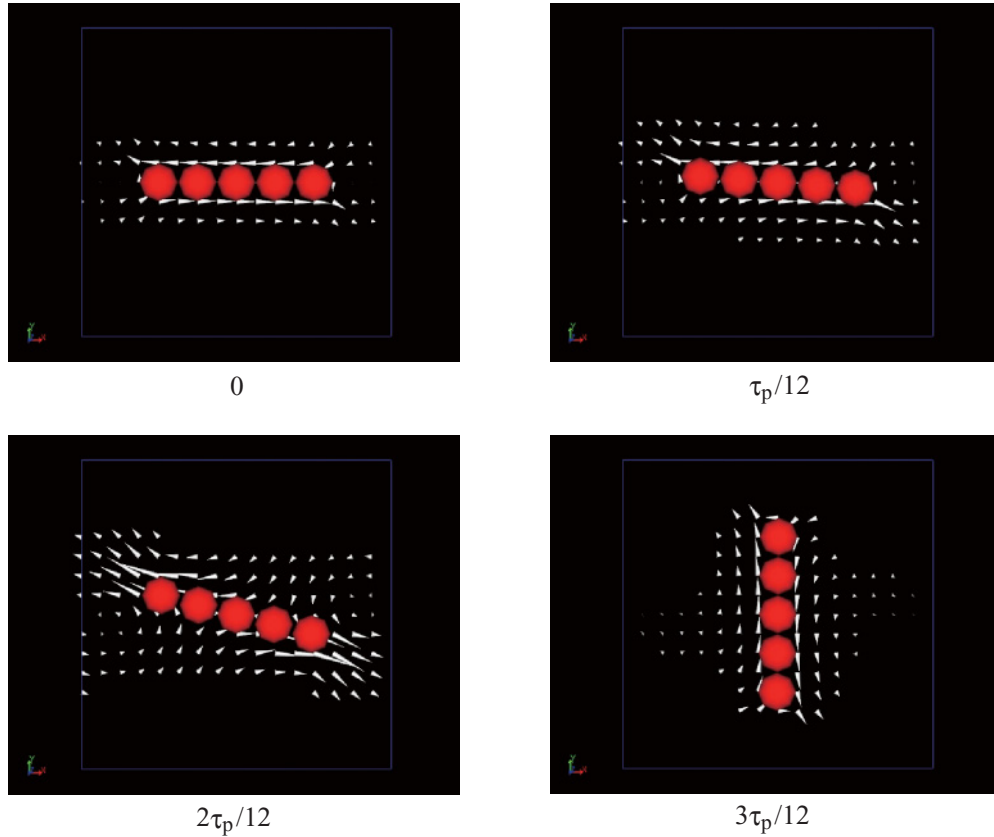
FIG. 5. (Color online) The time evolution of the deviation velocity field is $\mathbf{u}_d \equiv \mathbf{u} - \dot{\gamma}(y - L_y/2)\mathbf{e_x}$ at $k_B T = 0$. The times range from 0 to $\tau_p/4$, where τ_p is the rotational period. The velocity fields are plotted only when $|\mathbf{u}_d|/|\mathbf{u}| > 0.05$.

composed of many identical small beads. The shell model can be adequately modeled by decreasing the size of the beads.
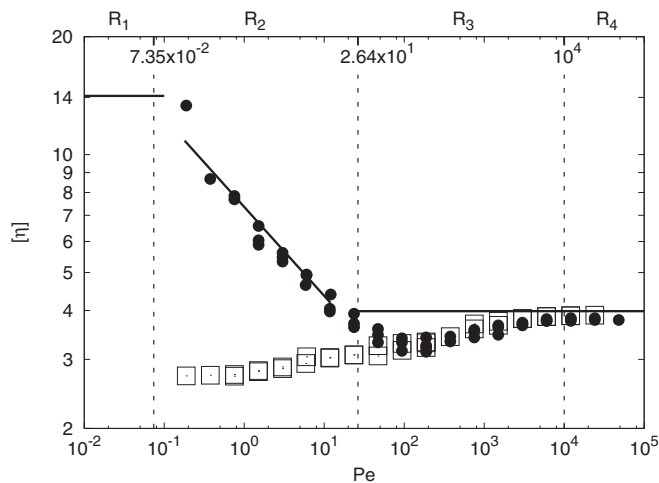

FIG. 6. The intrinsic viscosity as a function of Pe. $[\eta]$ (circle) and $[\eta_\theta]$ (square). The three solid lines correspond to the theoretical results of Hinch and Leal [5,6], with the first Newtonian regime denoted by R_1, the shear-thinning regime denoted by R_2, and the second Newtonian regime denoted by $R_3 + R_4$. In our simulation, the viscosity shows an undershoot before reaching the second Newtonian regime R_3.

From Eqs. (23) and (24), the relationship between $\dot{\gamma}/D_r$ and Pe is expressed as

$$\frac{\dot{\gamma}}{D_r} = \frac{l^3}{18[\ln l + d(l)]} \text{Pe}. \tag{26}$$

The theoretical model of Hinch and Leal is also plotted in Fig. 6 with the solid lines in the three different regimes, namely, the weak (R_1), intermediate (R_2), and strong ($R_3 + R_4$) shear regimes.

According to the work of Hinch and Leal [5], for the weak-shear regime $\dot{\gamma}/D_r \ll 1$, namely, Pe $\ll 7.35 \times 10^{-2}$, which is denoted by R_1 in Fig. 6, $[\eta]$ is constant. On the basis of Ortega's work [26], the intrinsic viscosity $[\eta]$ of the weak-shear flow regime for a rigid rod with a short aspect ratio is calculated as

$$[\eta] = \frac{4}{15} \frac{l^2}{\ln l + \Upsilon(l)}, \tag{27}$$

$$\Upsilon(l) = -0.90 - \frac{1.38}{l} + \frac{8.87}{l^2} - \frac{8.82}{l^3}. \tag{28}$$

This expression is identical to Hinch and Leal's result in the limit of $l \to \infty$. The lowest shear rate that we consider in the present simulations is still not in the weak-shear regime because of the extremely long simulation time needed to obtain reliable data.

For the intermediate shear regime $1 \ll \dot{\gamma}/D_r \ll l^3 + l^{-3}$, namely, $7.35 \times 10^{-2} \ll$ Pe $\ll 26.4$, which is denoted by R_2

in Fig. 6, the intrinsic viscosity $[\eta]$ shows shear-thinning as derived from Eq. (21),

$$[\eta] = C_1 \mathrm{Pe}^{-1/3} + 2B + 2/I_3, \qquad (29)$$

where C_1 is an arbitrary constant. Figure 6 shows good agreement between the data from the present simulation data and those of Hinch and Leal, where C_1 was determined to fit the simulation data. When l is sufficiently large, the contributions from the final two terms in Eq. (29) become negligible, and $[\eta] \propto \mathrm{Pe}^{-1/3}$.

For the strong-shear regime $l^3 + l^{-3} \ll \dot{\gamma}/D_r$, namely, $26.4 \ll \mathrm{Pe}$, which is denoted by R_3 and R_4 in Fig. 6, the theory predicts that the intrinsic viscosity $[\eta]$ is constant at $A\langle \sin^2 2\varphi \rangle_J + 2B + 2/I_3 = 3.99 = [\eta_\infty]$ from Eq. (21). In this case, $\langle \cdots \rangle_J$ denotes the ensemble average, which is calculated as

$$\langle f(\varphi) \rangle_J = \int_{-\frac{\pi}{2}}^{\frac{\pi}{2}} d\varphi f(\varphi) P_J(\varphi). \qquad (30)$$

We obtained $[\eta_\infty] = 3.82$ from our numerical data in the high shear regime, which is denoted by R_4 in Fig. 6. The error from the theoretical value 3.97 is within 4.26%.

For the regime $10^2 < \mathrm{Pe} < 10^3$, which is denoted by R_3 in Fig. 6, the behavior of $[\eta]$ shows a notable undershoot before reaching the high-shear limiting second Newtonian viscosity. This effect is attributable to the fluctuations in θ and gives rise to the deviations of $P''(\theta)$ from its high-shear limiting form $P^*(\theta) \equiv \int_{-\frac{\pi}{2}}^{\frac{\pi}{2}} P_J(\theta, \varphi) d\varphi$ and increases with decreasing Pe. The rods tend to align in the flow direction with increasing Pe. Therefore, $\langle \cos^4 \theta \rangle$ and $\langle \cos^2 \theta \rangle$ monotonically increase up to their high-shear limiting values with increasing shear rate. Increasing $\langle \cos^4 \theta \rangle$ and $\langle \cos^2 \theta \rangle$ leads to an increase in $[\eta]$ up to $[\eta_\infty]$ through Eq. (21). To examine the role of thermal fluctuations in θ in more detail, let us define

$$[\eta_\theta] = A\langle \sin^2 \varphi \rangle_J \langle \cos^4 \theta \rangle_\theta + 2B\langle \cos^2 \theta \rangle_\theta + \frac{2}{I_3} \quad (31)$$

$$= 1.81 \langle \cos^4 \theta \rangle_\theta + 0.12 \langle \cos^2 \theta \rangle_\theta + 2.02 \quad (32)$$

to estimate the contribution of θ fluctuations on the total intrinsic viscosity of the dispersion. In this case, $P(\varphi) = P_J(\varphi)$ is assumed in Eq. (21), and $\langle \cos^4 \theta \rangle_\theta$ and $\langle \cos^2 \theta \rangle_\theta$ are evaluated numerically from the present simulations. The results are plotted in Fig. 6 with the square symbols. One can see that the data of $[\eta_\theta]$ almost perfectly collapse onto those of $[\eta]$ for $10^2 < \mathrm{Pe}$.

However, the shear-thinning behavior observed for $10^2 > \mathrm{Pe}$ is attributable to the effect of the thermal fluctuations in φ. This behavior gives rise to the deviations of $P'(\varphi)$ from its high-shear limiting form $P_J(\varphi)$ and increases with decreasing Pe. To examine this effect quantitatively, we introduce

$$[\Delta \eta] \equiv [\eta] - [\eta_\theta] \qquad (33)$$

$$= A\langle \cos^4 \theta \rangle_\theta (\langle \sin^2 2\varphi \rangle_\varphi - \langle \sin^2 2\varphi \rangle_J) \qquad (34)$$

to eliminate the contribution of θ fluctuations from the total intrinsic viscosity of the dispersion. Figure 7 shows the behavior of $[\Delta \eta]$ as a function of Pe. $[\Delta \eta]$ decreases with increasing Pe, and finally $[\Delta \eta]$ goes to zero at approximately $\mathrm{Pe} \approx 150$. This value is considerably different from the value $\mathrm{Pe} = 26.4$
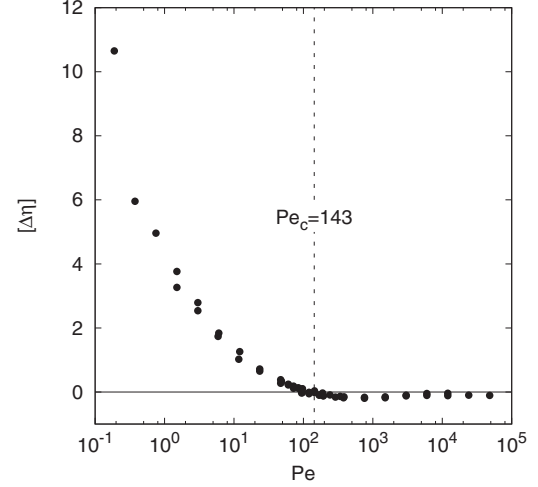
FIG. 7. The behavior of $[\Delta \eta]$ as a function of Pe. $[\Delta \eta]$ goes to zero at approximately $\mathrm{Pe} \approx 150$.

predicted by Hinch and Leal [5] for the viscosity transition from shear-thinning to the second Newtonian behavior but agrees well with our theoretical prediction of $\mathrm{Pe}_c = 143$, at which the dynamic crossover from Brownian to non-Brownian behavior occurs in the rotational motion of the rotating rod at $l = 7.1$ [27].

Figure 8 shows the first normal stress, $N_1 = (\sigma_{11}^{\mathrm{dis}} - \sigma_{33}^{\mathrm{dis}})$, normalized with respect to the viscous stress of the solvent, $\eta\dot{\gamma}$, as a function of Pe. According to Hinch and Leal [5], in the intermediate shear regime, denoted by R_2 in Fig. 8, the first normal stress behaves as $N_1 \propto \dot{\gamma}^{2/3} D_r^{1/3}$. Therefore, $N_1/\eta\dot{\gamma} \propto \dot{\gamma}^{-1/3} D_r^{1/3} \propto \mathrm{Pe}^{-1/3}$ in regime R_2. This behavior is in good agreement with our numerical results.

In the strong-shear regime, denoted by R_3 and R_4 in Fig. 8, the theory predicts a first normal stress of $N_1 = 0$. This is as given by Jeffrey's equation [1], which perfectly describes the
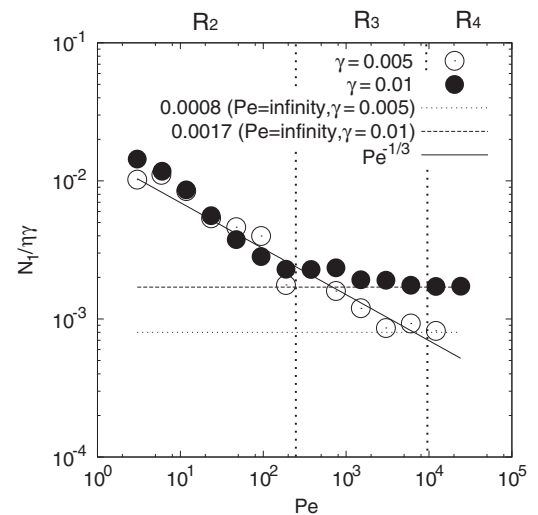
FIG. 8. Normalized first normal stress $N_1/\eta\dot{\gamma}$ as a function of Pe. $\dot{\gamma} = 0.01$ (closed circle) and $\dot{\gamma} = 0.005$ (open circle). The solid line corresponds to $\mathrm{Pe}^{-1/3}$, which is the theoretical result of Hinch and Leal [5,6]. The dashed (dotted) line corresponds to $N_1/\eta\dot{\gamma}$ in the limit that $\mathrm{Pe} \to \infty$ for $\dot{\gamma} = 0.01$ ($\dot{\gamma} = 0.005$).

tumbling motion in this regime. However, even if we assume $k_B T = 0$ so that Pe $\to \infty$, the numerical error in the first normal stress $E(\dot{\gamma})$ remains finite and depends on the shear rate. Nevertheless, because of this error, our results depart from the theoretical prediction of Hinch and Leal [5] for high Pe. We consider $E(\dot{\gamma})$ to be a numerical error arising from the competition between shear force and interbeads interaction, as described by Eqs. (10) and (11), when the rigid rod rotates in Jeffrey's orbit. Figure 8 shows $E(\dot{\gamma})$ for $\dot{\gamma} = 0.01, 0.005$, when Pe $> 10^4$, $E(\dot{\gamma})$ is in good agreement with $N_1/\eta\dot{\gamma}$ at each shear rate. This agreement is because the tumbling motion is well described by Jeffrey's equation [1].

Also of interest are the off-diagonal entries of the stress tensor and the second normal stress. However, these values are not accurately calculated by this numerical method. In comparison with theoretical results, the numerical error in the stress tensor σ_{12}^{dis} is near 4%. The other entries of the stress tensor are less than $0.01 \times \sigma_{12}^{dis}$. For example, the second normal stress, $N_2 \equiv \sigma_{22}^{dis} - \sigma_{33}^{dis} \approx 0.01 \times \sigma_{12}^{dis}$, is buried in numerical error.

IV. DISCUSSION

Let us discuss the numerical models with which the viscosity transition to the second Newtonian regime occurs based on Eq. (21). For the strong-shear regime $1 \ll \dot{\gamma}/D_r$, we can estimate $\langle \cos^2 \theta \rangle_\theta \simeq 1$ and $\langle \cos^4 \theta \rangle_\theta \simeq 1$ because $P_{\dot{\gamma}}(\theta, \varphi) \simeq P^*(\theta)P(\varphi)$. In this case $P(\varphi)$ satisfies the Fokker-Planck equation, shown as Eq. (15), for which the formal solution is given by

$$P(\varphi) = C_1 \int_0^\pi d\psi \exp\left[-\frac{\dot{\gamma}}{4D_r} f(\psi, \varphi)\right], \quad (35)$$

$$f(\psi, \varphi) = \psi - \left(1 - \frac{2}{l^2 + 1}\right) \sin\psi \cos(\psi - 2\varphi), \quad (36)$$

where C_1 is determined from the normalization condition, $\int_{-\frac{\pi}{2}}^{\frac{\pi}{2}} P(\varphi) d\varphi = 1$. When $\dot{\gamma}/D_r$ is sufficiently large, $P(\varphi)$ converges to $P_J(\varphi)$, represented by Eq. (14), and the viscosity displays second Newtonian behavior.

The above discussion is not valid for the limit of $l \to \infty$, which corresponds to an infinitely long or equivalently infinitely thin rod. In this limit the angular velocity of the tumbling rod becomes zero at $\varphi = 0$ from Eq. (17). Thus, the rod cannot continue its rotational motion without thermal fluctuations because the hydrodynamic torque acting on the rod becomes zero at $\varphi = 0$ for $l \to \infty$. Therefore, $P(\varphi)$ in Eq. (35) is modified to

$$P_\infty(\varphi) = C_2 \int_0^\pi d\psi \exp\left\{-\frac{\dot{\gamma}}{4D_r} [\psi - \sin\psi \cos(\psi - 2\varphi)]\right\}, \quad (37)$$

where C_2 is determined from the normalization condition, $\int_{-\frac{\pi}{2}}^{\frac{\pi}{2}} P_\infty(\varphi) d\varphi = 1$. Using Eq. (37), the intrinsic viscosity $[\eta]$
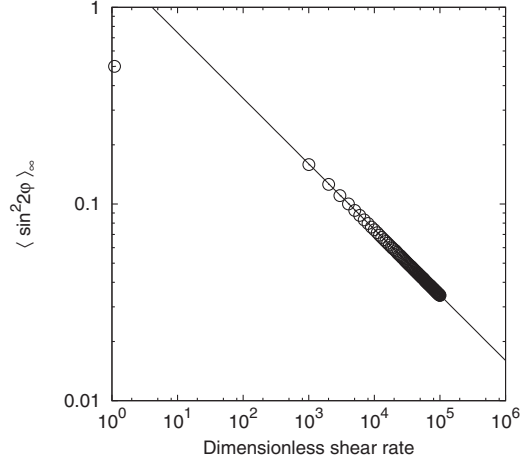
FIG. 9. The behavior of $\langle \sin^2 2\varphi \rangle_\infty$ as a function of $\dot{\gamma}/D_r$. Numerical results (circle). The solid line corresponds to $(\dot{\gamma}/D_r)^{-1/3}$

is rewritten as

$$[\eta] = A\langle \sin^2 2\varphi \rangle_\infty + 2B + 2/I_3, \quad (38)$$

$$\langle f(\varphi) \rangle_\infty = \int_{-\frac{\pi}{2}}^{\frac{\pi}{2}} d\varphi f(\varphi) P_\infty(\varphi). \quad (39)$$

It is demonstrated in Fig. 9 that the first term in Eq. (38) shows $\langle \sin^2 2\varphi \rangle_\infty \propto (\dot{\gamma}/D_r)^{-1/3}$ for the entire range of Pe. Figure 10 shows that only A is increasing with increasing l, while B and $2/I_3$ tend to be decreasing or constant with increasing l. We estimate $A/(2B + 2/I_3) \sim l^{1.8}$ for $l \to \infty$. This relational expression indicates that

$$[\eta] \propto \langle \sin^2 2\varphi \rangle_\infty \propto (\dot{\gamma}/D_r)^{-1/3} \quad (40)$$

holds for the entire range of Pe without indicating the occurrence of second Newtonian behavior. The same conclusion
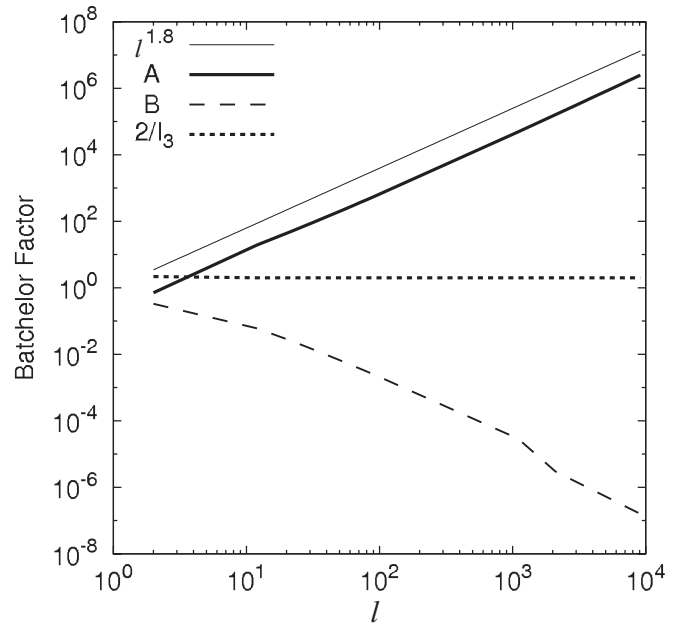
FIG. 10. The behaviors of A, B, and $2/I_3$ as a function of the aspect ratio l. A (bold solid line), B (dashed line), $2/I_3$ (dotted line). The thin solid line represents $l^{1.8}$.

can be derived by considering a characteristic shear rate $\dot{\gamma}^*$ at which the first term in Eq. (38) becomes comparable to the remaining terms. The condition is satisfied at

$$\frac{\dot{\gamma}^*}{D_r} \sim l^{5.4}. \tag{41}$$

Equation (41) indicates $\dot{\gamma}^* \to \infty$ for $l \to \infty$.

In the case of a previous numerical study [16], the hydrodynamic force acting on each bead particle was considered through the RPY tensor. Although the translational hydrodynamic force was properly considered, the rotational hydrodynamic torque acting on each bead particle was completely ignored in that study. Therefore, it is suspected that the hydrodynamic torque acting on the rod becomes zero at $\varphi = 0$. The rod cannot continue rotational motion at a high shear rate, where the effect of thermal fluctuations disappears. This situation is identical to the case of $l \to \infty$. We expect that the second Newtonian regime could be correctly reproduced with the RPY tensor approach if the hydrodynamic torque is properly taken into account.

V. CONCLUSION

In the present study, we numerically calculated the intrinsic viscosity $[\eta]$ of a dilute dispersion of rigid rods using a DNS method known as SPM. Simulations were conducted under the influence of thermal fluctuations and shear flow in the ranges of $5.0 \times 10^{-4} < k_{\mathrm{B}}T < 32$ and $5.0 \times 10^{-3} < \dot{\gamma} < 2.0 \times 10^{-2}$, respectively. We have successfully reproduced the viscosity transition from shear-thinning to the second Newtonian regime, as was correctly predicted by the theoretical model of Hinch and Leal [5,6].

However, some discrepancies were noted between the theoretical predictions and the results of the present simulations. By defining $[\Delta\eta]$ to eliminate the effects of fluctuations in θ, which is not considered in the theoretical model, we confirmed that the viscosity transition from shear-thinning to the second Newtonian behavior occurs at approximately Pe = 150. This value is considerably larger than the value of 26.4 predicted by Hinch and Leal [5] but agrees well with our theoretical prediction of $\mathrm{Pe}_c = 143$, at which the dynamic crossover from Brownian to non-Brownian behavior occurs in the rotational motion of the rotating rod [27].

We have analyzed the mechanism of the viscosity undershoot observed in our simulation before reaching the second Newtonian regime. Shear flow suppresses fluctuations in φ and θ as its rate is increased. The former contributes to decreasing $[\eta]$, but the latter contributes to increasing $[\eta]$. The undershoot occurs because of the two competing effects.

We also conclude that the viscosity transition to the second Newtonian regime can be reproduced correctly only if the hydrodynamic torque is properly taken into account in numerical models of the dispersions.

[1] G. B. Jeffrey, Proc. R. Soc. A **102**, 161 (1922).

[2] A. Peterlin and H. A. Stuart, Z. Phys. **112**, 1 (1939).

[3] V. H. Giesekus, Rheol. Acta. **2**, 50 (1962).

[4] G. K. Batchelor, J. Fluid Mech. **41**, 545 (1970).

[5] E. J. Hinch and L. G. Leal, J. Fluid Mech. **52**, 683 (1972).

[6] L. G. Leal and E. J. Hinch, J. Fluid Mech. **46**, 685 (1971).

[7] E. J. Hinch and L. G. Leal, J. Fluid Mech. **71**, 481 (1975).

[8] E. J. Hinch and L. G. Leal, J. Fluid Mech. **76**, 187 (1976).

[9] L. G. Leal and E. J. Hinch, Rheol. Acta **12**, 127 (1973).

[10] H. A. Scheraga, J. Chem. Phys. **23**, 1526 (1955).

[11] J. F. Ryder and J. M. Yeomans, J. Chem. Phys. **125**, 194906 (2006).

[12] H. Chen, Y. Ding, and A. Lapkin, Powder Tech. **194**, 132 (2009).

[13] G. Chauveteau, J. Rheol. **26**, 111 (1982).

[14] I. Noda, Y. Yamada, and M. Nagasawa, J. Phys. Chem. **72**, 2890 (1968).

[15] R. L. Christiansen and R. B. Bird, J. Non-Newtonian Fluid Mech. **3**, 161 (1977).

[16] D. Petera and M. Muthukumar, J. Chem. Phys. **111**, 7614 (1999).

[17] Y. Nakayama and R. Yamamoto, Phys. Rev. E **71**, 036707 (2005).

[18] Y. Nakayama, K. Kim, and R. Yamamoto, Eur. Phys. J. E **26**, 361 (2008).

[19] T. Iwashita, Y. Nakayama, and R. Yamamoto, J. Phys. Soc. Jpn. **77**, 074007 (2008).

[20] T. Iwashita and R. Yamamoto, Phys. Rev. E **79**, 031401 (2009).

[21] H. Kobayashi and R. Yamamoto, J. Chem. Phys. **134**, 064110 (2011).

[22] I. Pagonabarraga, B. Rotenberg, and D. Frenkel, Phys. Chem. Chem. Phys. **12**, 9566 (2010).

[23] A. Onuki, J. Phys. Soc. Jpn. **66**, 1836 (1997).

[24] M. M. Tirado and J. G. de la Torre, J. Chem. Phys. **73**, 1986 (1980).

[25] M. M. Tirado, J. Chem. Phys. **81**, 2047 (1984).

[26] A. Ortega and J. G. de la Torre, J. Chem. Phys. **119**, 9914 (2003).

[27] H. Kobayashi and R. Yamamoto, Phys. Rev. E **81**, 041807 (2010).